

# Optimization Design of the Integral Inertial Particle Separator Based on Response Surface Method

L. Zhou<sup>†</sup>, Z. Wang and J. Shi

*Shaanxi Key Laboratory of Internal Aerodynamics in Aero-Engine, School of Power and Energy, Northwestern Polytechnical University, Xi'an, Shan Xi Province, 710072, China*

<sup>†</sup>Corresponding Author Email: [zhouli@nwpu.edu.cn](mailto:zhouli@nwpu.edu.cn)

(Received February 22, 2019; accepted May 28, 2019)

## ABSTRACT

Inertial Particle Separator (IPS) is widely used as an important inlet protection device for turbo-shaft aero engine to protect the core engine in seriously polluted environment. In order to improve the separation efficiency of the IPS, an investigation was conducted to study the influence of critical geometrical and aerodynamic parameters on IPS performance, and Response Surface Method (RSM) was applied to explore the interaction between different parameters and obtain the response of the IPS performance on different parameters. Results show the separation of the sand particle in the IPS is achieved by the inertial accumulation of the sand particle, the trajectories of particles with small size are dominated by flow direction while paths of particles with larger size are dominated by the individual particle inertia and bounce characteristics from the IPS walls. The separation efficiency of the IPS is not only affected by the single geometrical parameters or aerodynamic parameter, but also apparently influenced by the interaction effects between different parameters. The most conspicuous influencing factor for the IPS separation efficiency on the AC-Coarse dust is  $Ma_{th}$  and the interaction effects between  $R_{o1}$  and  $Ma_{th}$ . IPS separation efficiency on the AC-Coarse dust is improved by 3.8% by multi-factors optimization based on RSM, and the sand particle with size larger than 8 micron can be completely separated.

**Keywords:** IPS; RSM; Separation efficiency; Geometrical parameter; Aerodynamic parameter.

## NOMENCLATURE

$e_N$	recovery coefficient of normal velocity component	$R_i$	radius of convex of the inner wall
$e_T$	recovery coefficient of tangential velocity component	$R_s$	radius of the splitter nose
$L_{o1}$	axial position of the outer wall	$R_{o1}$	radius of the outer wall
$L_s$	axial position of the splitter nose	$V_N$	normal velocity components
$Ma_{th}$	Mach number at the throat	$V_T$	tangential velocity components
$m_p$	total mass flow rate of sand particles	$\eta$	separation efficiency of the sand particles
$m_{c,p}$	mass flow rate of sand trapped at the outlet of the core flow passage	$\eta_C$	separation efficiency C-Spec sand
$m_{s,p}$	mass flow rate of sand trapped at the outlet of the scavenge flow passage	$\eta_{AC}$	separation efficiency for AC-Coarse dust
		$\sigma_c$	total pressure recovery coefficient

## 1. INTRODUCTION

Unlike the fixed-wing aircraft, which usually takes off and lands at well-equipped airports and flies at high altitudes for long time, the helicopter especially the attack helicopter named as “the

treetop killer”, often needs to take off and land frequently at sand-contaminated airstrips. Moreover, the attack helicopter generally undertakes long-time and low-altitude flights for better stealth, then large amounts of sand and foreign materials are raised by the downwash flow

of the rotor, which is easily ingested into the core engine by the intake device, resulting in deterioration of the helicopter engine performance. Therefore, the application of effective intake protection device on the turbo-shaft engine to supply clean air flow for the engine is of great significance to the operation of turboshaft engine when helicopters take off and fly in low-altitude sand-contaminated environment. Now, three kinds of inlet protection devices have been usually put into practice, including foreign object protection net, barrier filters and IPS. In contrast to other two inlet protection devices that are normally applied as airframe installed options, IPS system is designed as integral to the engine directly. This integrated design results in a more compact system, with advantages of high particle separation efficiency and reliable operation.

Massive investigations have been performed on the IPS (Saeed *et al.*, 2007; Al-Faris *et al.*, 2009; Barone *et al.*, 2015; 2018). Vittal (1986) summarized the design method of IPS, pointed out that the ratio of scavenge flow to core flow mainly impacted on the total pressure loss of the scavenge flow channel, and a vaneless IPS could achieve an efficiency of 85% on AC-Coarse dust with low total pressure loss at a scavenge flow of 16.3%. The application of Six Sigma design method to an IPS was presented by Frederic (2010), the influence of different factors on IPS separation efficiency and total pressure ratio were discussed. Results showed that the IPS design involved many parameters and their interactions could be accounted by Design of Experiments (DOE), response surfaces (surrogate models) and Pareto fronts. Hamed (1982) experimentally studied the influence of the vane and flow path of IPS on the separation efficiency, and got the relationship between the particle radius and the separation efficiency of IPS. Connolly (2016) discussed the effect of IPS particle separation efficiency as a function of scavenge leg geometry, and found that flow constriction with a hub-side ramp improved the separation efficiency. Investigation on a novel Outer Surface Geometry (OSG) for an IPS were conducted at a fundamental two-dimensional experiment facility (Connolly *et al.*, 2017). It showed the new OSG was successful to increase particle separation efficiency, particularly at low scavenge mass flow fraction. The newly defined parameter  $s/H$  (the ratio of scavenge channel height  $s$  to throat height  $H$ ) provided a convenient way to quickly estimate the expansion ratio of the scavenge channel and the potential for flow separation. Efficiency measurements were completed using different spherical particle sizes to isolate these effects on IPS separation efficiency for several IPS geometries (Barone *et al.*, 2013). Large size particles were shown to bounce through the IPS with near 100% efficiency. As particles size became smaller, their separation efficiency decreased due to the increasing fluid influences.

Ye (2007) introduced the flow path design method of the vaneless particle separator, the influence of the flow path characteristic on the total pressure

loss and separation efficiency were considered, results showed geometry parameters of the flow path were mutually dependent, and a good vaneless particle separator design should take into account the interaction among various parameters. Floria (2011) improved the flow path configuration of the IPS with the emphasis on increasing the separation efficiency and reducing the pressure loss simultaneously, where pressure coefficient and Reynolds number distribution in longitudinal and transverse sections of the scavenge flow exit were considered. The three-dimensional gas-solid two-phase flow field was numerically simulated to consider the influence of the intake and swirling vanes in the IPS with vanes. Separation efficiency was obtained for AC-Coarse dust and C-Spec sand (Dong *et al.*, 2008). It is found that separation efficiency increased with the growth of particle size. Effects of the air flow on particles were enhanced with the existence of the intake and swirling vanes, the smaller particles are easily ingested into the engine because of the aerodynamic force of core flow. Researches were conducted by Wu (2007) to find out effects of different factors on separation efficiency and total pressure loss, including inner walls, outer walls, wall curvature and the position of splitter. Results showed the separator efficiency of the IPS increased linearly when the inlet velocity and scavenge flow rate of IPS increased, so was the total pressure loss.

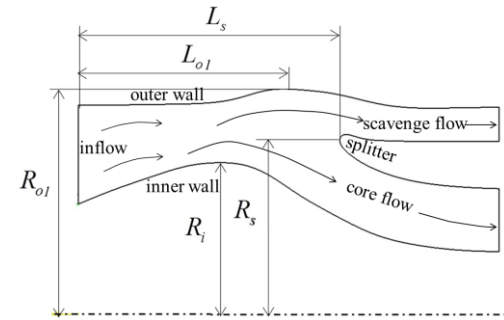
Now effects of aerodynamic and geometric parameters on the IPS performance have been investigated massively, but only single parameters are involved in most of work, furthermore, the interaction effects between different geometric parameters and aerodynamic parameters and their impacts on the IPS performance were not considered. In order to obtain the optimum performance of the IPS and provide the guidance for the IPS design, a typical IPS model was studied in this paper based on RSM, the effects of critical geometric and aerodynamic parameters on IPS performance were investigated, the mechanism of the flow field in the IPS was discussed, the relationship between the IPS performance and various factors were obtained, the interaction effects between different parameters were explored, and then multi-factor optimization with objective of maximum particle separation efficiency was carried out for the IPS, and the best parameter settings were determined.

## 2. GEOMETRICAL MODEL OF IPS

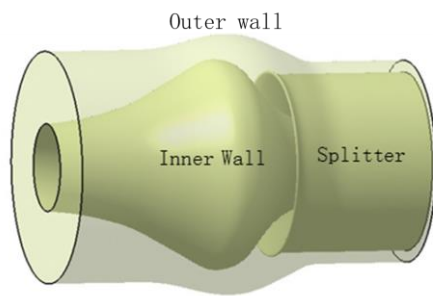
### 2.1 Basic Model and Critical Parameters

Figure 1 shows the sketch of the IPS structure, the main profile of the IPS includes the inner wall, the outer wall and the splitter wall. The flow channel formed by the walls converges firstly, the inner wall humps and its curvature is larger than the outer wall. Downstream of the throat, the flow channel is divided into two passages, where the air flow turns into the core flow passage, and particles will deflect from the main flow and be pumped out through the

scavenge flow passage, and thus particles are separated from the main flow path.



(a) 2D flow channel



(b) 3D model

**Fig. 1. Sketch of the structure of IPS.**

As shown in Fig. 1(a), geometrical parameters of IPS can be characteristic by the convex radius of the inner wall  $R_i$ , position parameters of the splitter which are axial position of  $L_s$  and radius of  $R_s$ , and position parameters of the outer wall which are radius of  $R_{o1}$  and axial position of  $L_{o1}$ . Where convex radius of the inner wall  $R_i$  determines the trajectory of sand particles downstream of the throat and the relative position of the splitter.

As the essential component of IPS, the splitter formed a bifurcated passage with the inner wall and outer wall, which are scavenge flow passage and core flow passage respectively. Most sand particles and a small fraction of the air flow enter the scavenge flow passage, with relatively clean air flowing into the core flow passage simultaneously. Thus, the axial position  $L_s$  and radius  $R_s$  of the splitter are critical geometrical parameters which can have impact on the particle separation efficiency.

Two aspects should be considered for the design of the IPS outer wall. Firstly, the function of the outer wall is to guide the flow with an appropriate trend. Secondly, from the view with good sand particles separation effectiveness, the outer wall needs to match the trend of the sand trajectory. Therefore,  $R_{o1}$  and  $L_{o1}$  should be carefully considered in the IPS design process.

Furthermore,  $Ma_{th}$  at the throat is a prominent aerodynamic parameter affecting the flow field and

separation efficiency of IPS, as the flow acceleration is decided by  $Ma_{th}$ , which has an important effect on the frictional loss and adverse pressure gradient at the inlet of the scavenge passage. Besides,  $Ma_{th}$  also directly contributes to the inertial force of the sand particle, and plays a decisive role in the separation effectiveness of sand particles

## 2.2 Performance Parameters of IPS

Performance of the IPS are represented by separation efficiency and total pressure recovery coefficient. Separation efficiency is an important parameter to quantify the separation effectiveness of the sand particle, which is defined as follows:

$$\eta = \frac{m_{s,p}}{m_p} = \frac{m_{s,p}}{m_{s,p} + m_{c,p}} \quad (1)$$

Total pressure recovery coefficient is used to evaluate the aerodynamic performance of the IPS, which is defined as the ratio of the averaged total pressure at the IPS outlet to the total pressure of the incoming flow.  $\sigma_c$  are adopted normally, with the expression as,

$$\sigma_c = \frac{P_{tc}}{P_{t0}} \quad (2)$$

## 3. COMPUTATION METHODOLOGY

### 3.1 Numerical Method

The simulation of flow field in the IPS involves the calculation of gas-solid two-phase flow. As the volume fraction of sand particles in the air flow is very small, it can be regarded as the sparse phase flow, which can ignore the influence of solid particles on air flow and the interaction between particles (Niu *et al.*, 2018; Liu *et al.*, 2008). Therefore, the gas-phase flow field and the solid-phase flow field are calculated separately. In this paper, the flow field in the IPS is numerically studied by Fluent software, with uncoupled calculation method performed, firstly, the gas-phase flow field is simulated, and then the trajectory of sand particles in the flow field is simulated by using Lagrange Discrete-Phase model. The flowfield with a typical vaneless IPS was calculated with SST (Shear Stress Transport)  $k-\omega$  model adopted as turbulence model (Yuan *et al.*, 2018), and good agreement was achieved between the prediction and experimental data. Thus, SST  $k-\omega$  model is chosen as the turbulence model in this paper. And the second-order upwind scheme is used to construct the spatial difference terms.

### 3.2 Collision Formula Between Sand Particles and Wall

Tabakoff (1985, 1991) put forward the functional relationship of the recovery coefficient between particles and walls, with the impact angle as the independent variable, which had been widely accepted.

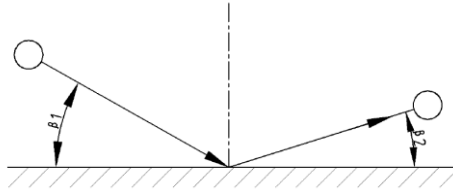


**Fig. 2. Sketch of Particle-Wall Collision.**

The collision formula between particle and wall in this paper is based on the theory proposed by [Tabakoff \(1985; 1991\)](#). As shown in Fig. 2, the recovery coefficient is mainly related to the impact angle, independent of the particle size and impact velocity. The detailed expression is as:

$$e_N = \frac{V_{N2}}{V_{N1}} = 1.0 - 0.0211\beta_1 + 0.0002278\beta_1^2 - 0.000000876\beta_1^3 \quad (3)$$

$$e_T = \frac{V_{T2}}{V_{T1}} = 0.953 + 0.000446\beta_1^2 - 0.00000648\beta_1^3 \quad (4)$$

where Superscript 1 and 2 represent the states before and after collision, respectively.

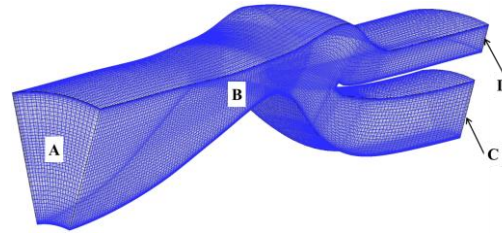
### 3.3 Particle Size Distribution of the Sand

Two kinds of standard sand with different particle size distributions are selected as reference, which are AC-Coarse dust (average particle size is 30 microns) and C-Spec sand (average particle size is 200 microns) respectively. These two kinds of standard sand are typically used for studies of foreign particle ingestion in the desert operation, and are composed of more than 90% SiO<sub>2</sub> quartz powder. The actual separation efficiency of the IPS is evaluated by calculating the separation effectiveness on these two kinds of sand particles, which are  $\eta_C$  for C-Spec sand and  $\eta_{AC}$  for AC-Coarse dust respectively.

### 3.4 Mesh and Boundary Condition

The geometric model of 1/12 IPS is selected as the calculation domain, and 1.5 times of the diameter difference between the internal wall and the external wall is extended upstream the IPS inlet. The three-dimensional structure mesh is displayed in Fig. 3. In order to meet the requirement of the turbulence model for near-wall mesh size and ensure the calculation accuracy, local refinement is carried out on the inner wall, outer wall and the splitter nose. The final mesh number is selected as 300,000 by the grid independence analysis.

In the calculation of gas-phase flow field, the inlet of the IPS is specified as pressure inlet boundary condition, total pressure, total temperature and flow angle are set. The outlet of core flow passage and scavenge flow passage is pressure outlet boundary condition, and the static pressure is given. The inner wall, outer wall and splitter walls of the IPS are described as adiabatic and non-slip wall boundary condition. The circumference of the model is set as periodic boundary conditions.



A: inlet boundary, B: periodic boundary, C and D: outlet boundary

**Fig. 3. Mesh and boundary condition.**

In the calculation of solid-phase flow field, the sand particles are uniformly projected from the IPS inlet plane. The walls are set as reflection-collision boundary, and relationships between recovery coefficients  $e_N$  and  $e_T$  with the collision angle are expressed in Eq. (3) and Eq. (4). Escape boundary and trap boundary are set at the core flow passage outlet and the scavenge flow passage outlet respectively. All particles accumulated at the core flow passage outlet are classified as escape, and all particles moving to the scavenge flow passage outlet are classified as capture. In this paper, the initial velocity of the particle projected is set as 50m/s, the mass rate and the density of the particle are 0.00015kg/s and 2650 kg/m<sup>3</sup>. Rosin-Rammler ([Tabakoff \*et al.\*, 1985; 1991](#)) distribution is used to approximate the particle size distribution of AC-Coarse dust and C-Spec sand. For AC-Coarse dust, the maximum particle radius is 0.2mm, the minimum particle radius is 0.005mm, and the averaged radius of the AC-Coarse dust is 0.049mm. For C-Spec sand, the maximum particle radius, the minimum particle radius and the averaged particle radius are 1mm, 0.063mm and 0.245mm respectively. The  $n$  index in Rosin-Rammler distribution are 0.92 and 1.82 for AC-Coarse dust and C-Spec sand.

### 3.5 RSM Approximate Modeling

In this paper, RSM is adopted to establish the approximate model of IPS performance and study the effect of the critical parameters of the IPS. RSM is a combination of mathematical and statistical methods, which is used to model and analyze the response of interested multiple variables ([Wang \*et al.\*, 2005](#)). The quadratic polynomial RSM is widely used, as it is characterized by simply modeling approach, excellent fitting accuracy and small computation cost. The principle of RSM approximate modeling technology is to establish the approximate model of the research through the selected samples, then replace the exact model by the approximate model for analysis. The procedure of RSM approximate modeling can be described as three parts: Design of Experiment (DOE), establishment of approximate model and optimal prediction for the response. Through the experiment design, the response values of each test point are obtained, and then the response problems affected by multiple variables are modeled and analyzed.

The first step of RSM is to find an appropriate approximation of the real functional relationship

between response  $Y$  and the set of independent variables. In order to obtain the coefficients of approximate polynomials, it is necessary to collect the response data by appropriate experimental design, and then use all sample points and their corresponding response values to effectively estimate the coefficients by the least square method.

The second step of RSM is to evaluate the fitting degree of the approximate polynomial to the real function relationship, which are obtained in the first step, and then determine the significance of each factor for the response. Commonly, a second order polynomial Eq. (5) is usually used.

$$Y = \alpha + \sum_{j=1}^k \beta_j x_j + \sum_{j=1}^k \gamma_j x_j^2 + \sum_{i=1}^{k-1} \sum_{j=i+1}^k \phi_{ij} x_i x_j \quad (5)$$

Where  $Y$  is the response variable,  $X(x_1, x_2, x_3, x_4 \dots x_k)$  are different influence factors,  $k$  is the number of influence factors,  $\alpha, \beta_j, \gamma_j, \phi_{ij}$  are coefficients of the polynomial. The polynomial coefficients  $\alpha, \beta_j, \gamma_j, \phi_{ij}$  are determined by means of a standard least-square regression which minimizes the sum of the square of the deviations for the predicted values from the actual ones for a set of points. And the validity of established approximate model is verified through different parameters. For the second-order model, the fitting degree is determined by  $R^2$  decision coefficient method. The  $F$  value method is usually used to detect the significance of each factor.

The third step of RSM is the optimal prediction for the response, that is, to determine the factors level according to the approximate model to get the optimum response.

#### 4. FLOW FIELD CHARACTERISTIC IN THE IPS

Flow field in the baseline IPS is shown in Fig. 4. For the IPS, in order to discharge the particle out of the engine through the scavenge flow passage, with less air flow sucked, the ratio of scavenge flow to core flow (SCR) is usually small. In this paper, SCR is chosen as 16%, the air flow rate in the scavenge passage is much smaller than that of the core flow passage in this case. Due to the convergent flow channel, the flow accelerates from the IPS inlet to the convex of the inner wall, and local pressure achieves the lowest value at the throat, then the pressure increases downstream, and the pressure in the scavenge flow passage is greater than that in the region between the throat and the splitter, as shown in Fig. 4(a). Therefore, the flow is routed by the splitter into the scavenge flow passage and the core flow passage respectively, the flow velocity in the scavenge flow passage decreases significantly due to the low SCR and the channel expansion caused by the outer wall profile, as shown in Fig. 4(b). From Fig. 4(c), as the entrance of the splitter plays a certain role in blocking the air flow, under the action of the inverse pressure gradient, a recirculation region inevitably appears near the

convex of the outer wall and the splitter nose, which is a typical flow characteristic in the IPS.

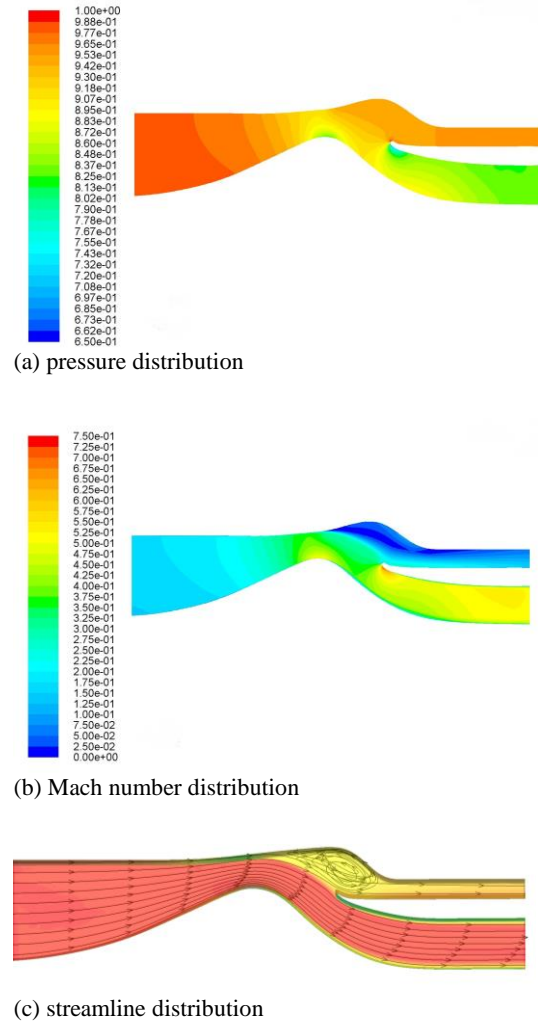


**Fig. 4. Flow Field in the Baseline IPS.**

The trajectory of sand particles in the flow field is simulated, and the sand mass flow rate trapped at the outlet of the scavenge flow passage and core flow passage are computed, the corresponding separation efficiencies of the baseline IPS for AC-Coarse dust and C-Spec sand are 75.2% and 98% respectively.

Figure 5 shows particles trajectories of AC-Coarse dust and C-Spec sand respectively. It can be found that the larger particle size of AC-Coarse dust and C-Spec sand are separated from the airflow direction after passing through the IPS throat. This is because particles trajectories with small particle size are dominated by flow direction, while paths with larger particle size are dominated by the individual particle inertia and bounce characteristics from the IPS walls. Under the action of the particle inertia, these larger particles collide with the wall continuously. After the collision reflection, except few particles enter the core flow passage, most particles enter the scavenge flow passage, and then

are excluded from the engine, achieving the separation of sand particles.

Compared with C-Spec sand, AC-Coarse dust contains more small-sized particles, such as sand particles size from 5 micron to 20 micron, which accounts for 38% of the total AC-Coarse dust. Because of its small inertia, the airflow force plays a decisive role in its trajectory, particles trajectories with small particle size are dominated by flow direction, leading to its tendency to follow the airflow. When sand particles pass through the IPS throat, particles trajectories of AC-Coarse dust are divided into two ways. As mentioned above, particles with larger size separates from the airflow and enters the scavenge flow passage under the action of its own inertia and collision reflection from the wall. Because of the relatively smaller inertia, the other particles with small size are dominated by flow direction, and enter the core flow passage. Therefore, most sand particles enter the scavenge flow passage and are excluded from the engine. Few sand particles with small size follow the air flow, and are routed into the core flow passage, eventually ingested into the engine. From the statistics of the separation efficiency under different size of sand particles, it shows AC-Coarse dust with particles size under 12 micron are nearly ingested into the engine.

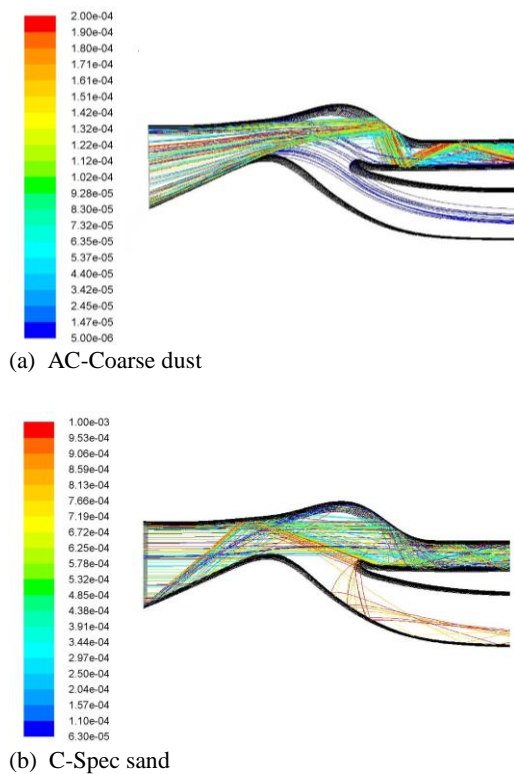


Fig. 5. Particle trajectory of different sand size.

## 5. IPS OPTIMIZATION BASED ON RSM

### 5.1 DOE of the IPS

As described above, critical geometrical parameters

of IPS consist of the convex radius of the inner wall  $R_i$ , position parameters of the splitter  $L_s$  and  $R_s$ , and the position parameters of the outer wall  $R_{ol}$  and  $L_{ol}$ . Furthermore,  $Ma_{th}$  at the IPS throat is a prominent aerodynamic parameter affecting the flow field and separation efficiency of IPS. Thus, these six parameters are considered in the optimization based on RSM approximate modeling.

From the result of the baseline IPS, the separation efficiency  $\eta_C = 98\%$  for C-Spec sand is acceptable, however, for the AC-Coarse dust, the separation efficiency  $\eta_{AC} = 75.2\%$  is relatively low.

Therefore, the separation efficiency  $\eta_{AC}$  for AC-Coarse dust is optimized in the following part.

According to the approximate modeling principle of RSM, the detailed procedures of the approximate modeling of IPS are as follows:

- 1) Determine the sample space of different parameters for the IPS, including independent variables and the range of the parameters. Six variables are chosen:  $R_i$ ,  $L_s$ ,  $R_s$ ,  $R_{ol}$ ,  $L_{ol}$  and  $Ma_{th}$ .
- 2) Select DOE method and perform the related experiment design. Here Box-Behnken Design (BBD) with rotatory is chosen for DOE, whose characteristic is that the distance between the other design points and the center point is equal, except for the center point.
- 3) Determine the concerned response variables. The response variables in this paper are separation efficiency  $\eta_{AC}$  for AC-Coarse dust and total pressure recovery coefficient  $\sigma_c$ . The corresponding response variables are obtained by performing simulation for the samples.
- 4) Ascertain the order of RSM objective functions and construct the fitting function. In this paper, quadratic polynomial model is chosen as the fitting function.
- 5) Complete the regress of polynomial coefficient by standard least-square, and perform significance analysis of each parameter by stepwise regression method, then remove unimportant factors and carry out polynomial coefficient regression again, finally execute the fitting examination of the model, i.e.  $R^2$  examination, which represents the ability of the response surface function to approximate the real value. When  $R^2$  is larger than 0.8, it denotes the fitting accuracy is acceptable and the approximate modeling is applicable. Otherwise, the design space of the selected variables should be adjusted, and the above process from 2) to 5) need be repeated.

Combined with the research object of this paper, the design space (range of each variable) is determined in Table 1, where all the parameters are non-dimensional-normalized. 6 involved factors and the

corresponding variable range are showed, based on the principles of the BBD design of experiment, a sample space with 54 points is generated which includes 49 factorial experiments and other 5 repeated experiments at the center point. And detailed samples with 54 points are not listed here due to the too large information of these samples.

**Table 1 DOE of the IPS**

Parameter	Value range			
	Value	2.52	2.72	2.92
$R_i$	Level	-1	0	1
	Value	3.68	3.88	4.08
$L_{oi}$	Level	-1	0	1
	Value	0.4	0.5	0.6
$Ma_{th}$	Level	-1	0	1
	Value	2.49	2.59	2.69
$R_s$	Level	-1	0	1
	Value	3.26	3.46	3.66
$R_{oi}$	Level	-1	0	1
	Value	3.87	3.97	4.07
$L_s$	Level	-1	0	1

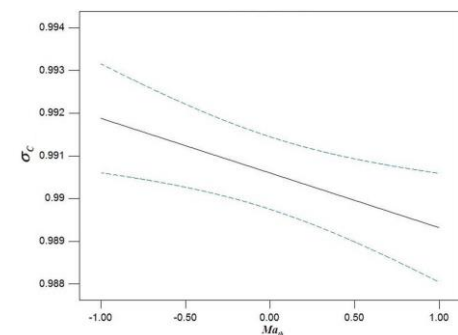
Typical ranges of value was assigned to critical parameters in Table 1 to study their effects on  $\eta_{AC}$  and  $\sigma_c$ , and for convenience, the range of every parameter is linearly conformed to [-1,1]. Numerical simulation of these related 54 models were performed to get  $\eta_{AC}$  and  $\sigma_c$ , and the flow field and the trajectory of sand particles are analyzed to discuss the influence mechanism of these critical parameters on IPS performance.

**5.2 Effects of  $Ma_{th}$  on IPS Performance**

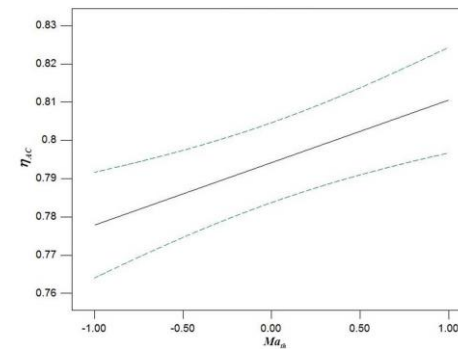
The distributions of  $\sigma_c$  and  $\eta_{AC}$  under different  $Ma_{th}$  are shown in Fig. 6, where the other five parameters are kept constant. It should be noted that the solid line represents the distributions of  $\sigma_c$  and  $\eta_{AC}$  under different  $Ma_{th}$ , it shows the linear effect of changing the level of a single factor  $Ma_{th}$ . It is constructed by predicting the responses for the low (-1) and high (+1) levels of  $Ma_{th}$ . The dashed lines in Fig. 6 are least significant difference (LSD) bar, which are the results of LSD calculation performed at the 95 percent confidence level in the samples space. The denotation of the solid line and dashed line in the following figures are same, which are not described further. It can be seen  $\sigma_c$  decreases with the increment of  $Ma_{th}$ , the magnitude of its reduction achieves 0.6%. But  $\eta_{AC}$  increases 3.3% when  $Ma_{th}$  changes from 0.4 to 0.6.

To analyze the phenomenon, the sand trajectory with particle size of 10 micron and streamline distribution are displayed in Fig. 7 and Fig. 8. When  $Ma_{th} = -1$ , the flow velocity is much smaller, so as

the corresponding momentum of the sand particle is. Due to the relatively small inertia, parts of the sand particles are dominated by the air flow, and are carried into the core flow passage. However, affected by the air flow with a larger velocity under  $Ma_{th}$  of 1, the sand particles obtain much larger momentum, the inertia of the sand particle becomes larger, and the potential for sand particles to break-away the air flow is increased, thus, most sand particles deflect from the air flow and enters the scavenge flow passage, and  $\eta_{AC}$  increases under the larger  $Ma_{th}$  correspondingly. Furthermore, when  $Ma_{th} = -1$ , a brunch of low energy flow recirculates into the core flow passage, resulting in a detrimental effect on  $\eta_{AC}$ , which does not happen under the case  $Ma_{th} = 1$ .



(a)  $\sigma_c$



(b)  $\eta_{AC}$

**Fig. 6. Variation of IPS performance parameters with  $Ma_{th}$ .**

It can be found in Fig. 8 that recirculation region appears near the scavenge flow passage inlet under these two  $Ma_{th}$ , being close to the convergent section of the outer wall, which is induced by the relatively small scavenge flow rate and its high local pressure. For the case  $Ma_{th}=1$ , besides the recirculation region near the scavenge flow passage inlet, a flow separation phenomenon also occurs near the inner wall, downstream the throat due to a large turning of the inner wall, and the corresponding total pressure loss increases under the effect of the strong viscous dissipation of this flow separation. Furthermore, the flow loss in the

IPS passage is proportional to the velocity, the larger  $Ma$  number is, and the larger flow loss is. Thus, the total pressure recovery coefficient  $\sigma_c$  decreases with the increase of  $Ma_{th}$ .

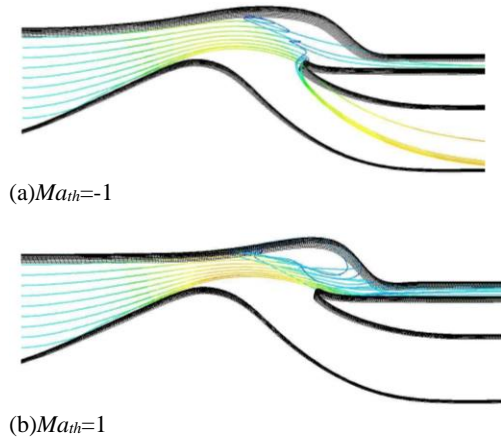


**Fig. 7. Sand trajectory distribution under different  $Ma_{th}$  (sand size=10 micron).**

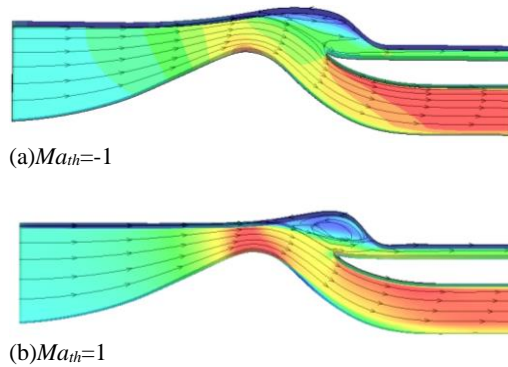


**Fig. 8. Streamline distribution under different  $Ma_{th}$  (sand size=10 micron).**

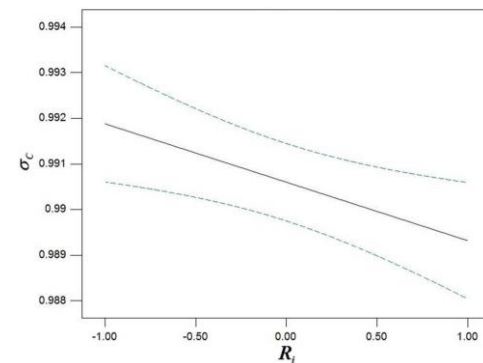
### 5.3 Effects of $R_i$ on IPS performance

The variation of IPS performance parameter with  $R_i$  is presented in Fig. 9, with other critical parameters kept as the initial design level of zero. The total pressure recovery coefficient  $\sigma_c$  decreases monotonously with the increase of  $R_i$ , and the reduction range is 0.26%. Separation efficiency  $\eta_{AC}$  increases by 6.4% with  $R_i$  increasing.

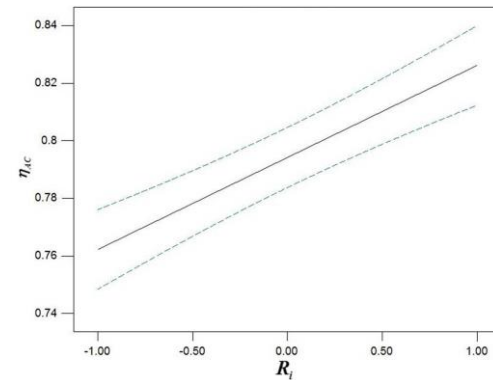
When is  $R_i$  under the level of 1, the inner wall is lifted up, and the position of the splitter remains unchanged, resulting in the more narrow core flow passage inlet between the inner wall and the splitter. The acceleration of the air flow is strengthened near the core flow inlet, a small supersonic region forms below the splitter nose, and flow separation occurs downstream the supersonic region. Thus, the total pressure recovery coefficient  $\sigma_c$  decreases under the larger  $R_i$ .

Figure 10 and Fig. 11 display the sand trajectory

and streamline distribution under different  $R_i$ , where sand size is chosen as 10 micron. For  $R_i = 1$ , the acceleration of the air flow is strengthened due to the IPS throat becomes smaller, and the larger velocity distribution in the IPS restrains the flow separation, inducing a smaller recirculation region near the inlet of the scavenge flow passage. The inertia of sand particle increases correspondingly due to the high velocity of the air flow under this case, the sand trajectory is trended to be decided by the sand particle inertia and the collision characteristic with the IPS wall, and the sand particle becomes easier to go into the scavenge flow passage. Also, the recirculation region near the scavenge flow passage is relatively smaller, making sand particles enter the scavenge flow passage more smoothly, and the sand particle in the recirculation region is not easy to be carried by the air flow with high velocity to enter the core flow passage. Furthermore, the trajectory of sand is forced to lift up when  $R_i$  increase, which is benefit for the sand particle to enter the scavenge passage. Thus, the separation efficiency  $\eta_{AC}$  is increased when  $R_i$  is the level of 1. On the other hand, as shown in Fig. 11, the recirculation region at the convex of the outer wall almost blocks the scavenge passage inlet under  $R_i$  of -1, which causes the sand recirculates into the core flow passage under the effect of the low-energy air flow, and the separation effectiveness of the sand particle is definitely deteriorated correspondingly.



(a)  $\sigma_c$



(b)  $\eta_{AC}$

**Fig. 9. Variation of IPS performance parameter with  $R_i$ .**

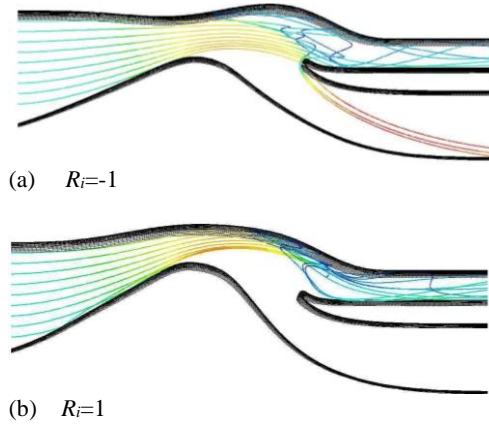


**Fig. 10. Sand trajectory distribution under different  $R_i$  (sand size=10 micron).**

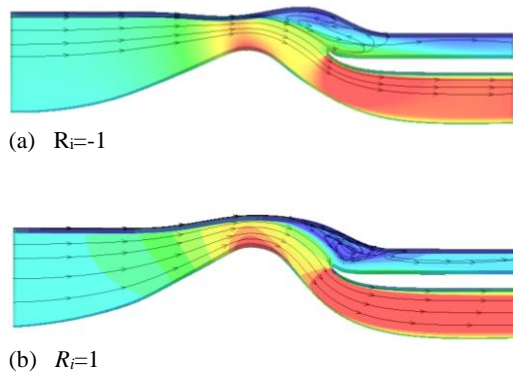


**Fig. 11. Streamline distribution under different  $R_i$  (sand size=10 micron).**

#### 5.4 Effects of $R_s$ on $\eta_{AC}$

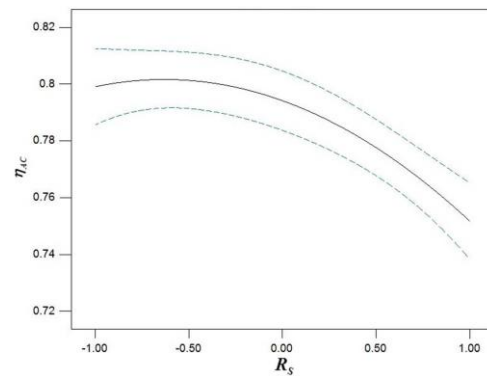
The change of separation efficiency  $\eta_{AC}$  with  $R_s$  is shown in Fig. 12. It can be seen that  $\eta_{AC}$  keeps almost constant firstly when  $R_s$  changes in the level range from -1 to 0, and then decreases by 5% from  $R_s$  level of 0 to  $R_s$  level of 1.

Figure 13 presents the streamline distribution under different  $R_s$ . As  $R_s$  increases, the splitter moves outward radically, the scavenge flow passage narrows gradually, and the core flow passage shifts up accordingly, thus, the core flow becomes closer to the accumulation zone of sand, then the sand particle is more easily wrapped into the core flow passage, and the corresponding separation efficiency  $\eta_{AC}$  decreases. When the level of  $R_s$  is -1 and 0, both of the recirculation zones are relatively larger for these two cases, which blocks the scavenge flow passage inlet and not beneficial to the separation of the sand particle, thus, the separation efficiency  $\eta_{AC}$  changes slightly for these two cases.

#### 5.5 Effects of $L_s$ on $\eta_{AC}$

The variation of  $\eta_{AC}$  with  $L_s$  is shown in Fig. 14.

$\eta_{AC}$  decreases as  $L_s$  increases, and the reduction amplitude achieves 2.8%. The splitter moves downstream with the increase of  $L_s$ , the expansion of the flow channel becomes larger, the velocity of the air flow decreases, and the inertial force of the sand particle reduces correspondingly. As the sand separation effectiveness of IPS depends on the inertial of the sand particle, when the splitter position moves downstream greatly, the inertial force of the sand particle is not large enough to smoothly enter the scavenge flow passage, and part of sand particles are entrained into the core flow passage, resulting in lower sand separation efficiency. Also, it can be observed from the streamline distribution in Fig. 15, part of the flow in the recirculation region which locates upstream the scavenge passage inlet, is carried by the core flow and enters the core flow passage under the case that  $L_s$  level is 1. This is detrimental to the separation effectiveness of the sand particle with small size, inducing the separation efficiency  $\eta_{AC}$  decrease further. Thus, the separation efficiency  $\eta_{AC}$  decreases with the increment of  $L_s$ .



**Fig. 12. Variation of  $\eta_{AC}$  with  $R_s$ .**

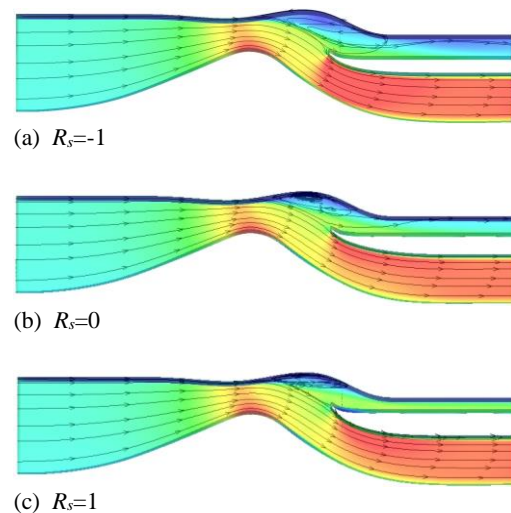


**Fig. 13. Streamline distribution under different  $R_s$  (sand size=10 micron).**

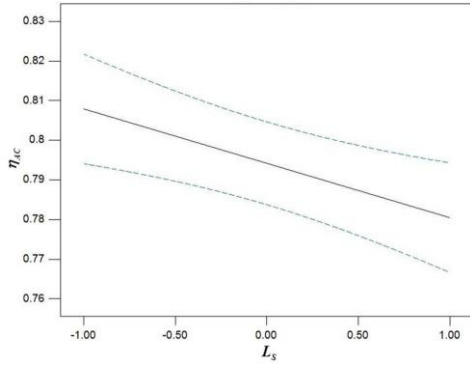
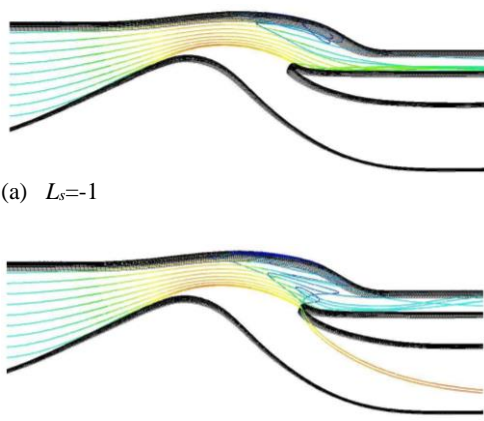


**Fig. 14.** Variation of  $\eta_{AC}$  with  $L_s$ .



(a)  $L_s = -1$   
(b)  $L_s = 1$   
**Fig. 15.** Streamline distribution under different  $L_s$  (sand size=10 micron).

### 5.6 Interaction Effects Between Different Parameters

According to the simulation results of these 54 samples, the response surface model based on a second-order polynomial is created as follows:

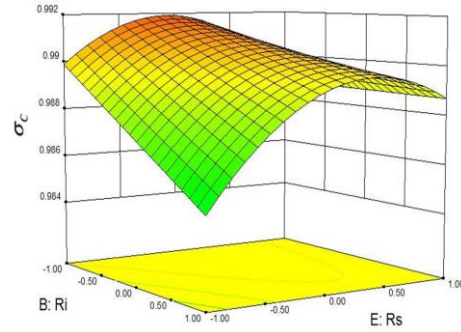
$$\begin{aligned} \sigma_c = & -1.28 - 0.0168Ma_{th} - 0.0033R_i + 0.006R_{O1} \\ & + 0.0309R_s + 2.43 \times 10^{-5}R_i \cdot R_s \\ & - 4.6 \times 10^{-5}R_{O1} \cdot R_s - 0.0001R_s^2 \end{aligned} \quad (6)$$

$$\begin{aligned} \eta_{AC} = & -32.81 - 5.416Ma_{th} + 0.0739R_i \\ & + 0.0159R_{O1} + 0.1044L_{O1} + 0.2927R_s - 0.0027L_s \\ & + 0.0323Ma_{th} \cdot R_{O1} - 0.00023R_i \cdot R_{O1} \\ & - 0.00023R_i \cdot R_s - 0.00037L_{O1} \cdot R_s \\ & - 0.00014L_{O1}^2 - 0.00075R_s^2 \end{aligned} \quad (7)$$

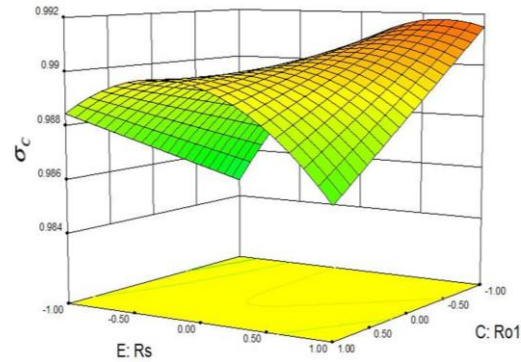
where every variation has been transformed to its real unit.

From the obtained response surface equation of  $\sigma_c$  and  $\eta_{AC}$ , the relationships between the IPS performance and various parameters are clearly described. Except for the influence of each critical parameter, the total pressure recovery coefficient  $\sigma_c$  is conspicuously influenced by interaction

effects between  $R_i$  and  $R_{O1}$ ,  $R_i$  and  $R_s$ . Interaction effects between  $Ma_{th}$  and  $R_{O1}$ ,  $R_i$  and  $R_{O1}$ ,  $R_i$  and  $R_s$ ,  $L_{O1}$  and  $R_s$  have impact on the separation efficiency  $\eta_{AC}$  for the AC-Coarse dust. Thus, the interaction effect between different two parameters cannot be ignored in the design process of the IPS.



(a)  $R_i$  and  $R_s$



(b)  $R_i$  and  $R_{O1}$

**Fig. 16.** Influence of interaction effect on  $\sigma_c$ .

Figure 16 shows influence of interaction effect between  $R_i$  and  $R_s$ ,  $R_s$  and  $R_{O1}$  on the total pressure recovery coefficient  $\sigma_c$ . It clearly displays the different variation trend of  $\sigma_c$  with  $R_i$  under different  $R_s$  level. When the level of  $R_s$  is -1, that is under smaller  $R_s$ , the core flow passage inlet located between the inner wall and the splitter is relatively narrow as compared with the baseline IPS, and the narrowing of the core flow passage inlet becomes more obvious with the increase of  $R_i$ . The acceleration of the air flow is apparently strengthened near the core flow inlet, with the supersonic region formed below the splitter nose, thus,  $\sigma_c$  decreases with the increment of  $R_i$ . Under  $R_s$  level of 1, although the core flow passage inlet is narrowed with the increase of  $R_i$ , the air flow can easily enter the core flow passage due to the upward moving splitter nose,  $\sigma_c$  only changes slightly with the change of  $R_i$  under larger  $R_s$ . Thus, the interaction effect between  $R_i$  and  $R_s$  obviously exists for their effect on  $\sigma_c$ . Under the interaction effect

between  $R_i$  and  $R_s$ , the peak of  $\sigma_c$  is achieved at  $R_s$  level of 0 and  $R_i$  level of -1.

Similarly, the prominent interaction effect between  $R_s$  and  $R_{o1}$  is displayed in Fig. 16(b),  $\sigma_c$  distribution with  $R_{o1}$  shows the contrary tendency under different level of  $R_s$ , and the peak of  $\sigma_c$  appears when  $R_{o1}$  level is -1 and  $R_s$  level is 1 respectively.

The interaction effect between  $Ma_{th}$  and  $R_{o1}$  is shown in Fig. 17. As  $Ma_{th}$  increases, the inertia force of the sand particle becomes larger, so is the separation efficiency  $\eta_{AC}$ , which is shown by  $R_{o1}=1$ . However, when  $R_{o1}=-1$ , the outer wall moves downward along the radial direction, enhancing the tendency of downward deflection of the air flow, although the momentums of the air flow and sand particles increase with the increment of  $Ma_{th}$ , the air flow and sand particles tends to enter the core flow passage under the restriction of the downward moved outer wall, and the separation efficiency  $\eta_{AC}$  correspondingly decreases as  $Ma_{th}$  increases. The streamline under different  $Ma_{th}$  is given in Fig. 18, which shows the recirculation region underneath the convex of the outer wall is larger under  $Ma_{th}$  level of 1, thus the blockage to the scavange flow passage is stronger, which causes the separation efficiency  $\eta_{AC}$  to be decreased. As a result, when the level of  $R_{o1}$  are -1 and 1 respectively, the change of  $\eta_{AC}$  with  $Ma_{th}$  is different, which is absolutely affected by the interaction effect between  $Ma_{th}$  and  $R_{o1}$ .  $\eta_{AC}$  reaches its peak value under high level of 1 for both  $Ma_{th}$  and  $R_{o1}$ .

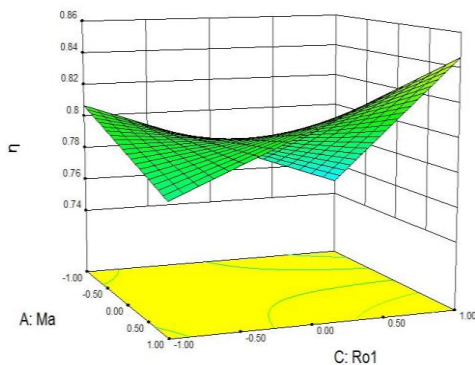


Fig. 17.  $Ma_{th}$ - $R_{o1}$  interaction effect on  $\eta_{AC}$ .

The interaction effect between  $R_s$  and  $L_{o1}$  is shown in Fig. 19. The inlet of the scavange flow passage becomes narrower when  $R_s$  increases, the sand particle is not easy to enter the scavange flow passage, so the separation efficiency  $\eta_{AC}$  decreases, which is shown by  $L_{o1}$  level of 1. However, when  $L_{o1}=-1$ , the outer wall moves

upward as compared with the baseline IPS, the inevitably appeared recirculation region moves upward accordingly, a blockage effect forms for the air flow and sand particles under this case, thus the separation efficiency  $\eta_{AC}$  becomes smaller as compared with other larger  $L_{o1}$ , and  $\eta_{AC}$  is mainly restricted by  $L_{o1}$ , then there is no obvious change on the separation efficiency  $\eta_{AC}$  as  $R_s$  increases. The streamline is shown in Fig. 20, which shows the recirculation region underneath the convex of the outer wall grows larger when  $R_s$  increases, easily blocking the flow scavange passage, which weakens the effects of  $R_s$  on the separation efficiency  $\eta_{AC}$ . As a result, when the level of  $L_{o1}$  are -1 and 1 respectively, the change of  $\eta_{AC}$  with  $R_i$  is different, which is influenced by the interaction effect between  $R_s$  and  $L_{o1}$ .

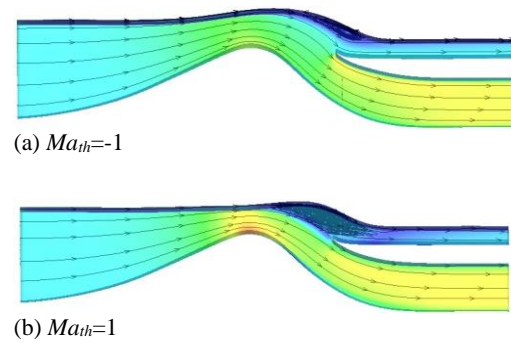


Fig. 18. Comparison of streamline under different  $Ma_{th}$  level ( $R_{o1}=-1$ ).

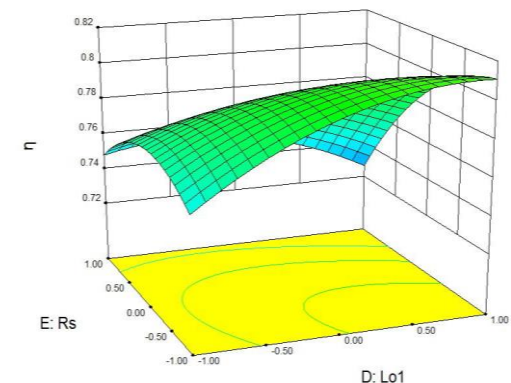


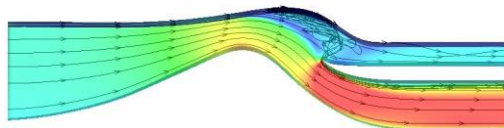
Fig. 19.  $R_s$  - $L_{o1}$  interaction effect on  $\eta_{AC}$ .

### 5.7 Optimization Design of the IPS

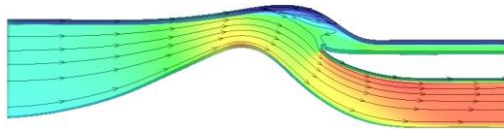
According to the response surface equations of total pressure recovery coefficient  $\sigma_c$  and separation efficiency  $\eta_{AC}$ , the relationship between the IPS performance and major parameters can be clearly

displayed, and the IPS performance also can be evaluated quickly for any parameter setting. Furthermore, based on the obtained response surface equation of  $\sigma_c$  and  $\eta_{AC}$ , optimization of the IPS can be carried out to seek the best combination of parameters.

In this paper, the optimization of the IPS is to determine the optimum parameter settings with the optimization target of the maximum  $\eta_{AC}$ , considering the excellent aerodynamic performance simultaneously. According to the response surface model based on a second-order polynomial, optimized values for the critical parameters are showed in Table 2. Compared with the baseline IPS model,  $R_i$  increases to lift up the inner wall, the outer wall shifts downward along the radial direction and moves downstream, and the splitter moves upstream.



(a)  $L_{o1}=-1$



(b)  $L_{o1}=1$

**Fig. 20. Comparison of streamline on periodic section as  $L_o$  increases ( $R_s=-1$ ).**

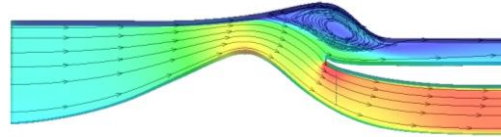
**Table 2 parameter settings before and after optimization**

	$R_i$	$R_{o1}$	$L_{o1}$	$R_s$	$L_s$
after optimization	2.92	3.26	3.94	2.58	3.89
before optimization	2.72	3.69	3.88	2.59	3.97

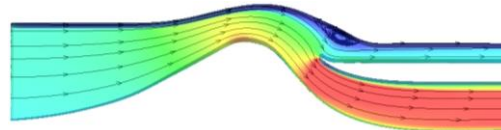
The optimized IPS model is numerically simulated, and the obtained total pressure recovery coefficient  $\sigma_c=0.986$ , separation efficiency  $\eta_{AC}=83.2\%$ . Compared with the baseline model, the separation efficiency for AC-Coarse dust  $\eta_{AC}$  increases by 3.8%, moreover, the separation efficiency for C-Spec sand  $\eta_C=98.5\%$ .

Figure 21 presents the comparison of the streamline between baseline IPS and optimized IPS model, an increased  $R_i$  can increase the flow velocity at the throat, and increase the inertia force of sand particle, making the sand particle easily deflect from the core flow. Furthermore, the optimized values for  $R_{o1}$  and  $L_{o1}$  decrease the recirculation region, ensure the sand particle smoothly enter the scavenge flow passage, and reduce the probability

of the recirculation of sand particle into the core flow passage. After the optimization of the IPS, the sand particle with size larger than 8 micron can be completely separated and discharged from the scavenge flow passage, while only the sand particle size larger than 12 micron can be realized the complete separation before optimization.



(a) streamline of baseline model



(b) streamline of optimized model

**Fig. 21. Comparison of streamline between baseline model and optimized model.**

## 6. CONCLUSION

Numerical investigation was performed for the IPS based on RSM, the effects of different parameters on IPS performance and flow field were explored, conclusions are as follows:

- 1) The separation of the sand particle in the IPS is completed by the inertial accumulation of the sand particle, the trajectories of particles with small size are dominated by flow direction, while paths of particles with larger size are dominated by the individual particle inertia and bounce characteristics from the IPS walls. For the effectiveness of the sand particle separation,  $Ma_{th}$  demonstrates the inertia force of sand particles.  $R_i$  represents the radial position of the throat, which provides a height potential for the separation of sand particles.  $R_s$  and  $L_s$  have decisive effect on the distance between the sand particles and the splitter.  $R_{o1}$  and  $L_{o1}$  have definite effect on the recirculation region size and flow pattern, and have an important effect on the blockage of the scavenge flow passage.

$\eta_{AC}$  increases with the increment of  $Ma_{th}$ ,  $R_i$  and  $L_{o1}$ .  $\eta_{AC}$  decreases as  $R_s$  and  $L_s$  increases.

- 2) The separation efficiency  $\eta_{AC}$  for the AC-Coarse dust, is not only influenced by  $L_s$ ,  $Ma_{th}$ ,  $R_i$  and  $R_s$ , but also influenced by interaction effects between  $Ma_{th}$  and  $R_{o1}$ ,  $R_i$  and  $R_{o1}$ ,  $R_i$  and  $R_s$ ,  $L_{o1}$  and  $R_s$ . The most conspicuous influencing factor for  $\eta_{AC}$  is  $Ma_{th}$  and the interaction effect between  $R_{o1}$  and  $Ma_{th}$ . Interaction effects between different factors should be incorporated into the design of the IPS.

- 3) Using the obtained RSM model for the IPS, the design of the IPS can be guided, optimization of the IPS can be carried out to seek the best combination of parameters, achieving the maximum total pressure recovery coefficient  $\sigma_c$  and separation efficiency  $\eta_{AC}$ , and performance evaluation can also be quickly performed for any parameter setting. An optimized IPS model is obtained with the parameter setting of  $R_i=2.92$ ,  $R_{o1}=3.26$ ,  $L_{o1}=2.94$ ,  $R_s=2.58$ ,  $L_s=3.89$ , and the separation efficiency  $\eta_{AC}$  for AC-Coarse dust is increased by 3.8%, the sand particle with size larger than 8 micron can be completely separated.

#### ACKNOWLEDGEMENTS

The author(s) disclosed receipt of the following financial support for the research, authorship, and/or publication of this article: The authors would like to express their gratitude for the financial support of the National Natural Science Foundation of China (No. 51876176, 51576163), MIIT and Natural Science Basic Research Plan in Shaanxi Province of China (2019JM-135).

#### REFERENCES

- Al-Faris, E. F. and F. Saeed (2009). Design and optimization method for inertial particle separator systems. *Journal of Aircraft* 46(6), 1119-1129.
- Barone, D., E. Loth and P. H. Snyder (2015). Efficiency of an inertial particle separator. *Journal of Propulsion and Power* 31(4), 997-1002.
- Barone, D., E. Loth and P. H. Snyder (2018). Flow field and efficiency of a two-dimensional inertial particle separator, *Journal of American Helicopter Society* 63(1), 1-9.
- Barone, D., J. Hawkins, E. Loth and P. Snyder (2013). Inertial particle separator efficiency using spherical particles. In *49<sup>th</sup> AIAA/ASME/SAE/ASEE Joint Propulsion Conference*, San Jose, USA, AIAA 2013-3666.
- Connolly, B. J., E. Loth and C. S. Frederic (2017). Novel outer surface geometry for an inertial particle separator. In *53<sup>rd</sup> AIAA/SAE/ASEE Joint Propulsion Conference*, Atlanta, USA, AIAA 2017-5053.
- Connolly, B. J., E. Loth, P. H. Snyder, and C. S. Frederic (2016). Influence of scavenge leg geometry on an inertial particle separator. In *54<sup>th</sup> AIAA Aerospace Sciences Meeting*, California, USA, AIAA 2016-1596.
- Dong, X. T. and S. F. Wang (2008). Numerical simulation of three-dimensions two-phase flow in inlet particle separator with vanes. *Machine Tools and Hydraulics* 36(10), 136-139
- Floria, P., Y. Fu, T. Wang and C. G. Gu (2011). Improvement method of an inlet particle separator based on stream lines analysis. *Fluid Machinery* 39(4), 10-16, 53
- Frederic, C. S. (2010). Six Sigma methods applied to an inlet particle separator design. In *13<sup>th</sup> AIAA/ISSMO Multidisciplinary Analysis Optimization Conference*, Texas, USA, AIAA 2010-9398.
- Hamed, A. (1982). Particle dynamics of inlet flowfields with swirling vanes. *Journal of Aircraft* 19(9), 707-712.
- Saeed, F. and A. Z. Al-Garni (2007). Analysis method for inertial particle separator. *Journal of Aircraft* 44(4), 1150-1158.
- Tabakoff, W. (1991). Measurement of particles rebound characteristics on materials used in gas turbines. *Journal of Propulsion and Power* 7(5), 805-813.
- Tabakoff, W. and M. F. Malak (1985). Laser measurements of fly ash rebound parameters for use in trajectory calculations. In *Gas Turbine Conference and Exhibit*, Texas, USA, ASME paper 85-GT-161.
- Vittal, B., D. Tipto and W. A. Bennett (1986). Development of an advanced vaneless inlet particle separator for helicopter engine. *Journal of Propulsion and Power* 2(5), 438-444.
- Wang, Y. F. and C. G. Wang (2005). The application of response surface methodology. *Journal of the CUN (Natural Sciences Edition)* 14(3), 236-240.
- Wu, H. G. (2007). *Characteristic study on vaneless integral particle separator*. Master Thesis, Nanjing University of Aeronautics and Astronautics, Nanjing, China
- Ye, J., B. A. Hu and Y. Xiong (2007). Flow path design of vaneless particle separator for turbo shaft engine. *Journal of Modern Machinery* 138(2), 39-4.